JOURNAL OF PROPULSION AND POWER
Vol. 18, No. 6, November–December 2002

Casting Process Impact on Small-Scale Solid Rocket Motor Ballistic Performance

P. Le Breton* and D. Ribéreau†
SNPE Propulsion, 33166 Saint Médard en Jalles Cedex, France

It has been widely reported that the ballistic response of solid rocket motors depends on the process used to manufacture it. Usually, the empirical parameters necessary to predict the performance of a motor (hump effect and scale factor), linked to the manufacturing process, are deduced from the exploitation of previous firing tests. The physical phenomena linked to those empirical parameters are sought to simulate directly the ballistic behavior of a new motor, in the future. One step in these studies has been to manufacture, with the same propellant, several small-scale grains, using three casting processes, and to study the influence of the manufacturing process on the ballistic behavior. Some of those grains have been fired, and others have been cut in several samples for local measurements of burning rate. The main results of experimental analysis are the profile of the radial burning rate on the web coherent with the hump effect, the strong ratio between radial and axial burning rates on each point of the web, and the visualization of propellant stratification by nuclear magnetic resonance (NMR) imaging due to the casting method. The experimental results have then been compared to a numerical simulation performed using a new code developed at SNPE to compute surface burnback with varying burning rate. In this mathematical model, the propellant should not be homogeneous as it is in constant burning rate simulations. The nature and the form of the heterogeneity are linked to the casting method. They may be deduced from a casting simulation performed at SNPE with the MONTREAL® code or from NMR imaging. The simulation results are very close to experimental results in terms of hump effect, scale factor between two casting processes, local burning rate profiles, and local anisotropy of propellant.

I. Introduction

FOR many years, SNPE has expended an important effort in the improvement of ballistic performance predictions of large solid rocket motors (SRMs) for both space and strategic propulsion.[1–4] One of the main investigation fields is the study of the impact of the manufacturing process on the ballistic response of the SRM. It is now acknowledged that the ballistic performance of solid rocket motors depends on the process used to manufacture it.[5,6] Two types of impact are studied.

The first impact is macroscopic and results because the filling of large grain motors requires several batches of propellant. If there is a great difference in burning rate between batches, even if it is acceptable according to the specification, it becomes necessary to take into account the real value of each mix in the surface burnback computation particularly for the prediction of combustion tail off. This is done by our new three-dimensional code BALISTE®,[7] in which the three-dimensional shape of mixes interfaces is deduced from a three-dimensional grain filling simulation.

The second impact of the manufacturing process on ballistic performance concerns a smaller scale and is due to particle segregation in the propellant during the filling. This heterogeneity of propellant leads to operating particularities such as the hump effect and a large part of the scale factor. The impact of the manufacturing process on ballistic performance is the subject of several studies at SNPE. These studies concern the mechanisms of formation of heterogeneity, their characterization, and their integration in ballistic predictions.[8–11,20] This last item has lead to the development of two new numerical tools. The first one is a varying burning rate surface burnback computation code, which is described in this paper. To be able to integrate the result of this computation in ballistic performance prediction, it has also been necessary to develop a new ballistic performance prediction code. In the code MOPTI, the ballistic performance is simulated by linking time step by time step the varying surface burnback simulation to a two-dimensional computational fluid dynamics (CFD) simulation in the combustion chamber. This paper presents a study concerning the impact of propellant burning rate anisotropy on ballistic performance. A small grain has been defined to study the impact of process on ballistic performance. Several grains have been manufactured with three different processes. One grain for each process has been fired, and another one has been cut in samples for local characterizations. The new varying burning rate surface burnback code has been used to simulate the performance of each grain. The results obtained for both firing tests and local measurements have been compared to the simulation results.

Received 14 August 2001; revision received 23 May 2002; accepted for publication 5 June 2002.

*Space Propulsion Program Manager, B.P. 57.
†Grain Design Manager, B.P. 57.

II. Description of the Study

A. Experimental Study

The grain we have chosen for this study is presented on Fig. 1. The grain is inhibited on his external diameter. Six grains have been manufactured in the same propellant batch hydroxyl-terminated polybutadiene/ammonium perchlorate/aluminium (HTPB/AP/Al 14/68/18) using three different processes: 1) process A, one-point rotating casting around the mandrel, 2) process B, one-point rotating casting without mandrel, and 3) process C, three equally spaced points casting around the mandrel.

Three of these grains have been fired, and the three others have been cut in samples for local characterizations. The local characterizations consist of burning rate and nuclear magnetic resonance (NMR) imaging visualizations.

Two experimental techniques have been used for the burning rate measurements: strand burner and ultrasonic measurements. In the strand burner technique, the sample has a parallelepiped form ($1 \times 1 \times 7$ cm) inhibited on all its faces except one end. The combustion is initiated in a pressurized tank and the combustion time between the two ends is measured. The mean burning rate on the entire length of the sample (7 cm) is deduced.

The sample used for ultrasonic measurements is a cylinder (diameter of 60 mm and thickness of 30 mm). The periphery is inhibited, and one face is connected to the ultrasonic sensor. The combustion is initiated on the other face. The sample is burned in an open bomb. This measurement gives the evolution of the sample's thickness and of the pressure in the bomb vs time. Then, the evolution of burning rate vs sample thickness for a given pressure is deduced. For this transformation, the pressure sensitivity is assumed invariant. It is justified because, in an open bomb, the pressure does not present a strong variation (between 4 and 6 MPa). The experimental results show that the pressure exponent does not vary from one process to another for a given batch of propellant and for a small pressure variation.

The first technique uses smaller samples and thus enables more numerous and more local measurements. On the other hand, this method is less precise than the ultrasonic technique. Another advantage of the ultrasonic technique is it provides the evolution of the burning rate along the web and not just a mean value like the strand burner technique.

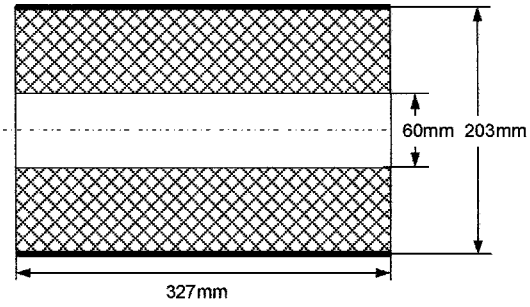

Fig. 1 Silvan grain.

In the following, we distinguish the radial and the longitudinal burning rates. The first one corresponds to the burning rate along the web, and the second one is parallel to the bore. Using the ultrasonic technique, we are able to measure the burning rate profile along the web and its evolution on the height of the grain as shown in Fig. 2 for the grains manufactured using the rotating casting. With the three-points casting, only radial burning rate profiles are measured under the casting points and in the knit line (Fig. 3).

In Figs. 2 and 3, we also show the positions of strand burner samples. In the grains manufactured by rotating casting, this technique is used to measure the longitudinal burning rate profile along the web and the mean radial burning rate. For the three-points casting, a radial burning rate profile is also measured around the circumference. In Figs. 2 and 3, the combustion direction of the samples is plotted. Combustion starts at the inner bore of radial samples and at the bottom of longitudinal samples.

B. Numerical Study

The performance of this grain has been simulated using a varying burning rate surface burnback code developed by SNPE.[12] In our model (Fig. 4), the burning rate on one point of the combustion area depends on the local angle α between the combustion front and a physical parameter characteristic of the propellant flow organization. The propellant flow organization is the gray curve in Fig. 4a. The burning rate V has a minimum value V_{min} for an angle of 0 deg and a maximum value V_{max} for an angle of 90 deg (see Fig. 4b).

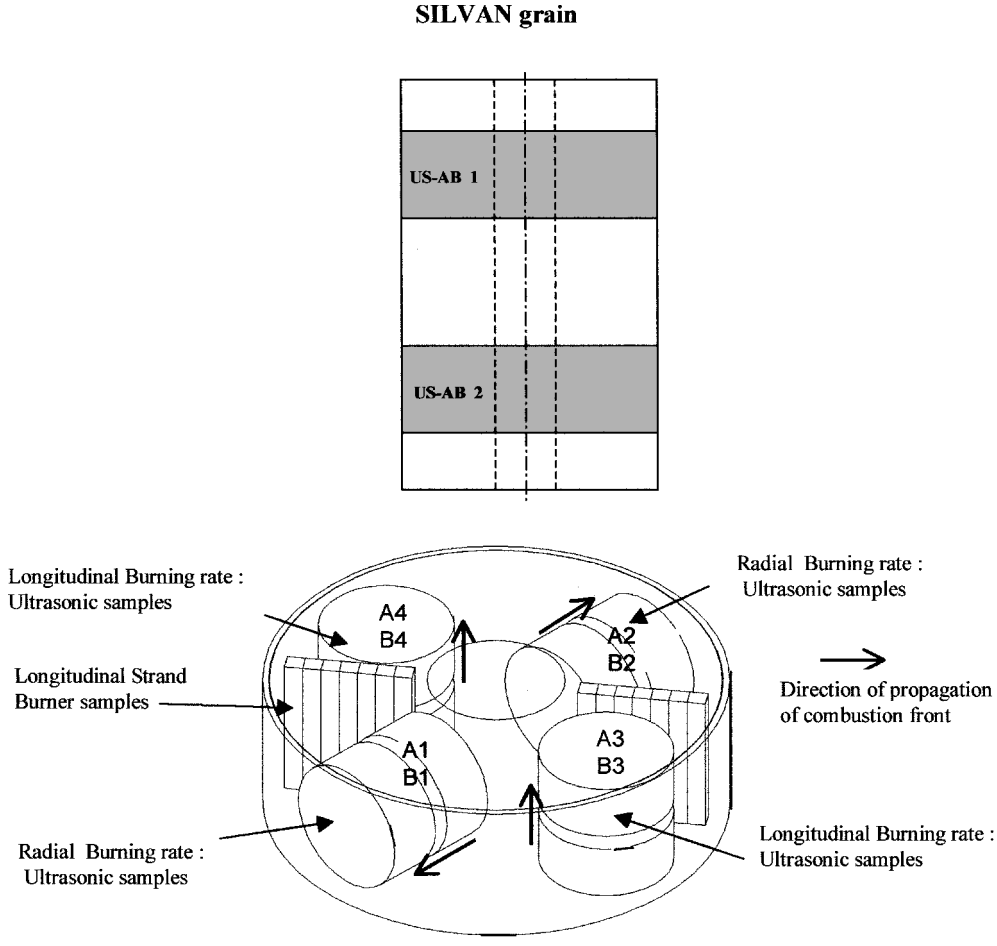

Fig. 2 Cutaway drawing of a Silvan grain: location of burning rate samples (rotating casting, A and B processes).

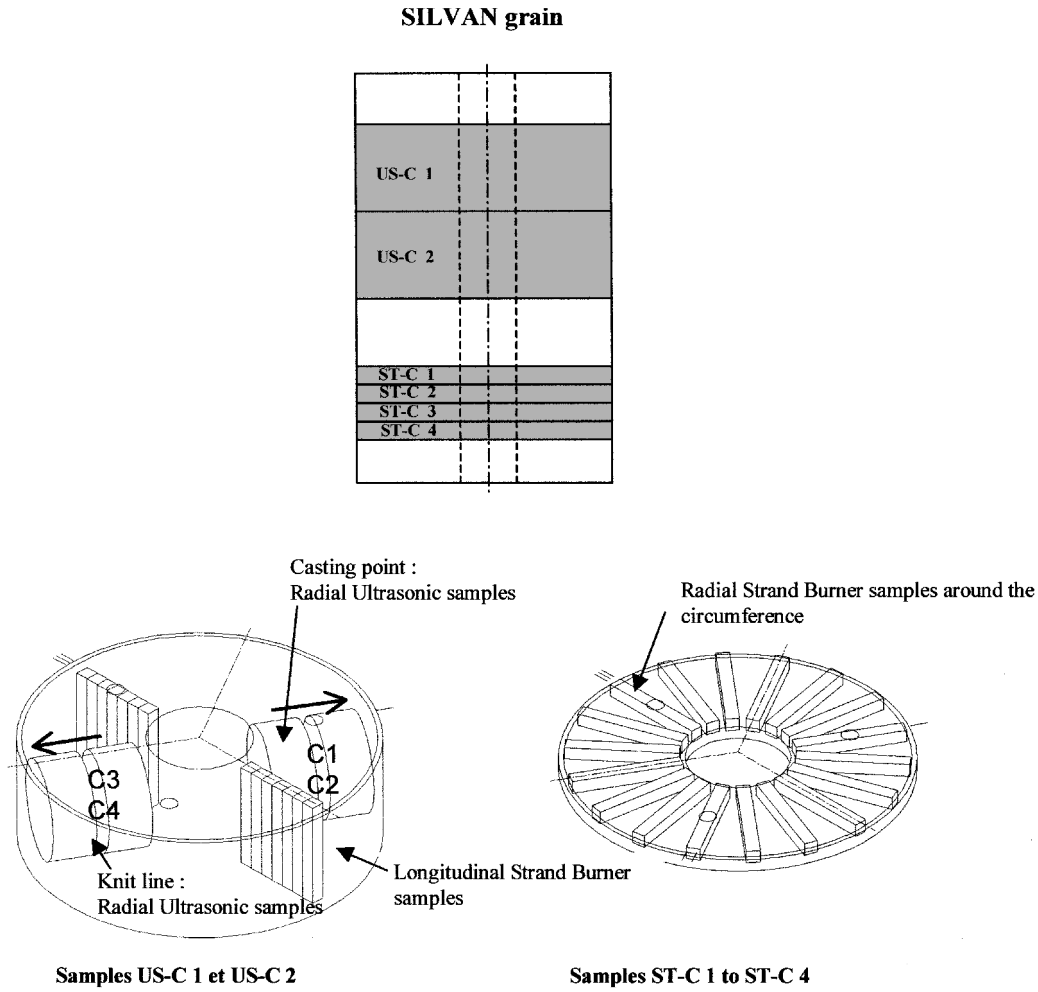

Fig. 3 Cutaway of a Silvan grain: location of burning rate samples (three-points casting, C process).

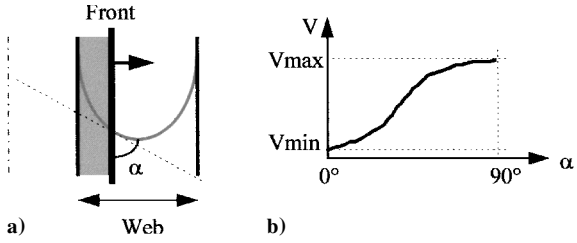

Fig. 4 Link between propellant heterogeneities and burning rate.

In this section, we briefly describe the numerical algorithm[13–16] used to compute the front position in the media shown in Fig. 4. The computational domain is Ω. The boundary is divided in two parts: Γ_0, which is inhibited, and Γ_1, which is the location of the uninhibited points. We assume $\partial\Omega = \Gamma_0 \cup \Gamma_1$, so that the boundary points are either inhibited or uninhibited.

We describe the location of the front at time t by the isovalue $t = \Psi(x, y)$, $(x, y) \in \Omega$. This can be justified by mathematical arguments, provided that $R(\alpha)$, the burning rate for an angle α, is regular enough and stays strictly positive:

$$\begin{aligned} -1 + R[\alpha(\nabla\psi, \nabla\theta)]\|\nabla\psi\| &= 0, \qquad t \rangle 0, \qquad x \in \Omega \\ -1 + R[\alpha(\nabla\psi, \nabla\theta)]\|\nabla\psi\| &\geq 0, \qquad t \rangle 0, \qquad x \in \Gamma_1 \\ \psi(x, y) &= 0, \qquad \forall (x, y) \in \Gamma_0 \end{aligned} \tag{1}$$

In Eq. (1), the physical parameter characteristic of the propellant flow organization is defined by $\theta(x, y) = cte$. In Eq. (1), we explicitly give the relation between the front shape ψ and the propellant flow organization θ.

This equation is a stationary Hamilton–Jacobi (HJ) equation. The numerical procedure we use relies on ideas widely used within the CFD community. We look for the solution of Eq. (1) as the steady solution of the HJ equation:

$$\begin{aligned} \psi_t - 1 + R[\alpha(\nabla\psi, \nabla\theta)]\|\nabla\psi\| &= 0, \qquad x \in \Omega, \qquad t \rangle 0 \\ \psi(x, y, t = 0) &= 0, \qquad x \in \Omega \\ \psi(x, y, t) &= 0, \qquad x \in \Gamma_0, \qquad t \rangle 0 \\ \psi(x, y, t) &= +\infty, \qquad x \in \Gamma_1, \qquad t \rangle 0 \end{aligned} \tag{2}$$

The parameter t has no physical meaning, it is only an iteration parameter. The solution of Eqs. (1) and (2) must be searched in the class of viscosity solutions.

The computational domain is discretized in two dimensions with a triangular mesh. We denote by T any current triangle and M any mesh point. The discretization of Eq. (2) is carried out via the scheme

$$\psi_M^0 = 0$$

$$\psi_M^{n+1} = \psi_M^n - \Delta t\left[-1 + R(M)H\left(M, p_{i_1}^n, \ldots, pi_M\right)\right] \tag{3}$$

In Eq. (3), the numerical Hamiltonian H is an approximation of $\|\nabla\psi\|$, known as the Godunov Hamiltonian. Its arguments are the gradients of the piecewise linear interpolation of ψ^n on the mesh. The range $p_{i_1}^n, \ldots, p_{i_M}$ is the list of the gradients for all of the triangles having M as vertex. $R(M)$ is an approximation of $R[\alpha(\nabla\psi, \nabla\theta)]$; it is sufficient to have an approximation of α that is the average angle at node M. A remarkable point of this algorithm is that the boundary conditions of Eq. (2) are automatically contained in the numerical Hamiltonian H (Refs. 1 and 3).

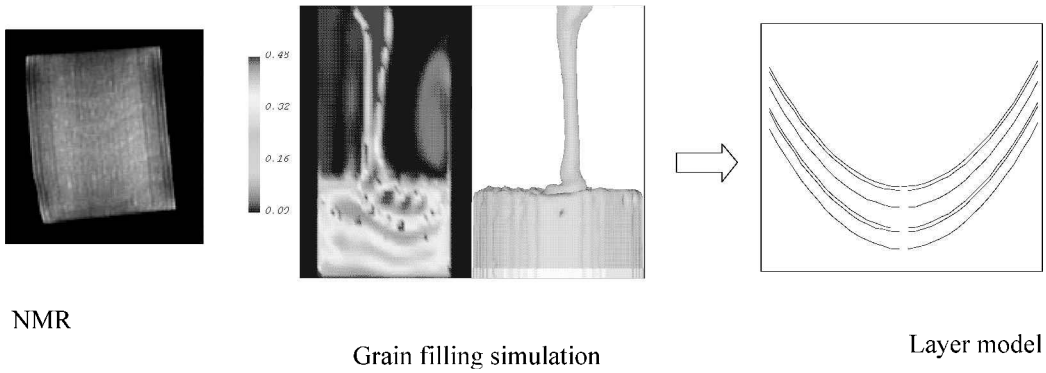

Fig. 5 Shape of flow organization (rotating casting with mandrel).

The time step Δt is computed via the Courant–Friedrichs–Lewy CFL like condition $\Delta t/h \leq 1$, where h is the maximum diameter of the triangles T. The convergence of this explicit scheme can be improved by using a local time stepping as in CFD.

The shape of the propellant flow organization is deduced from grain filling simulations performed using the SNPE code MONTREAL® in which a segregation model has been integrated and from NMR imaging.

MONTREAL code has been developed to simulate grain filling, both for small and large grains. It is built around a finite volume technique to solve the Navier–Stokes equations for incompressible fluids and simulates particle transfer in suspensions:

$$\rho_m\left(\frac{\partial \boldsymbol{u}}{\partial t} + \boldsymbol{u}.\nabla \boldsymbol{u}\right) = -\nabla p + \rho \boldsymbol{g} + \nabla \cdot \left[\eta_m \nabla \boldsymbol{u} + \nabla \boldsymbol{u}^t\right] \quad (4)$$

$$\operatorname{div} v = 0 \quad (5)$$

The symbol ρ_m is the density of the suspension and its viscosity η_m is modeled through the Krieger correlation (See Ref. 17):

$$\eta_m = \eta_s(1 - \phi/\phi_m)^{-1.82} \quad (6)$$

In Eq. 6, η_s is the solvent viscosity, $\phi_m = 0.68$ the maximum particle concentration in the suspension, and ϕ the unknown concentration, which satisfies the advection–diffusion equation proposed by Phillips et al.,[18]

$$\frac{\mathrm{d}\phi}{\mathrm{d}t} + v \cdot \operatorname{grad}\phi = a^2 K_c \operatorname{div}(\phi^2 \operatorname{grad}\dot{\gamma} + \phi\dot{\gamma} \operatorname{grad}\phi)$$

$$+ a^2 K_\eta \operatorname{div}\left[\frac{\phi^2\dot{\gamma}}{\eta_m}\frac{\partial \eta_m}{\partial \phi} \operatorname{grad}\phi\right] \quad (7)$$

where $\dot{\gamma}$ is the rate of strain tensor, a is the particle diameter, and K_c and K_η are empirical constants. Equation (7) is semi-empirical; it is based on that particles migrate from high shear rate to low shear rate regions. Empirical constants K_c and K_η have been determined from experimental measurements of the concentration profiles in Couette and Poiseuille flows (see Ref. 19).

The exploitation of those results suggests a mathematical model based on a periodic organization made of three layers (Figs. 5 and 6); layer 1, propellant overconcentrated in ammonium perchlorate (AP); layer 2, propellant underconcentrated in AP; and layer 3, mean composition. Each layer i has a thickness e_i, a burning rate r_i, and a density d_i and is supposed to be homogeneous. The burning rate value for each layer is adjusted to obtain the best agreement between numerical and experimental results. Our mathematical model is two dimensional in its present state. This is the reason why only the two-dimensional processes have been simulated in this study.

In the following, we present the experimental results obtained for the three manufacturing processes and the comparison with numerical results in the two cases presented in Figs. 5 and 6.

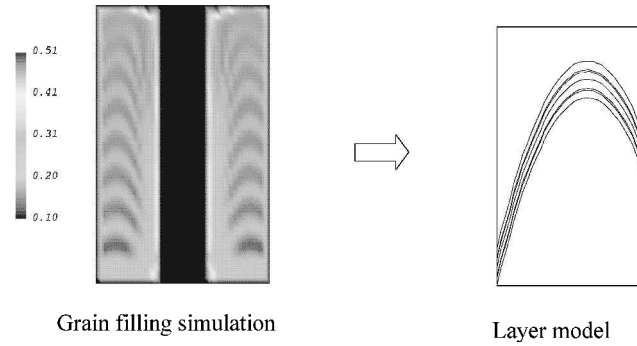

Fig. 6 Shape of flow organization (rotating casting without mandrel).

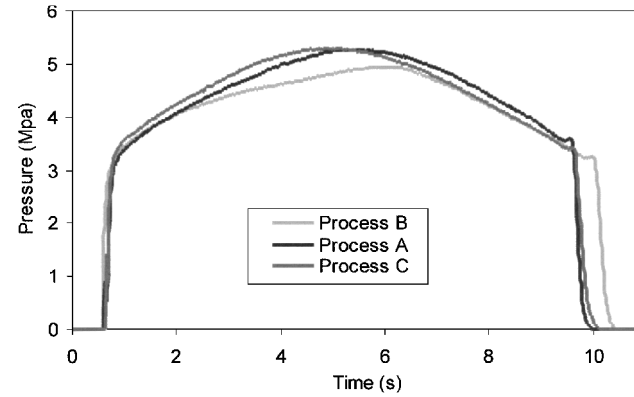

Fig. 7 Firing tests results.

III. Presentation of Numerical and Experimental Results

A. Experimental Results

The experimental results are of two types. The first one corresponds to the global behavior of the motor and is represented by the hump effect and the mean burning rate deduced from firing tests exploitation. The hump effect is the ratio between the experimental and the theoretical pressure vs time evolutions. The second experimental data set corresponds to a local behavior and is deduced from local measurements.

Figure 7 shows the evolution of pressure obtained during firing tests for each process. Those curves show that the behavior of the grains is different, at first from a qualitative point of view (hump effect) and then from a quantitative point of view (mean value of burning rate : scale factor).

Table 1 gives the corresponding values of mean burning rate. The mean burning rate value is deduced from the pressure evolution using a classical mass balance method:

$$r_b = w_b \cdot p/Ip_t \quad (8)$$

Table 1 Mean values of burning rate

Parameter	Process A	Process B	Process C
Mean burning rate, mm/s	7.55	7.28	7.48
Ratio with process B (experience)	1.037	1	1.0275
Ratio with process B (simulation)	1.032	1	——

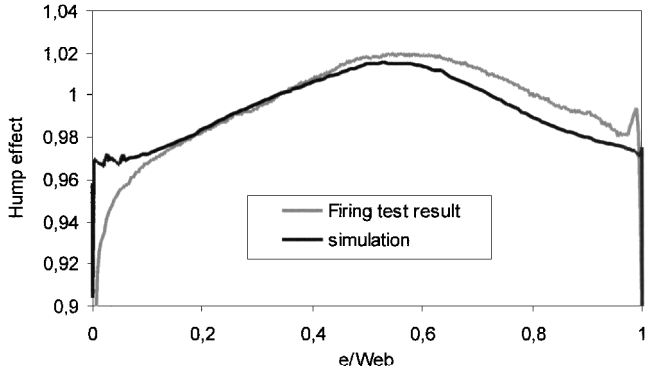

Fig. 8 Process A, hump effect (firing test result).

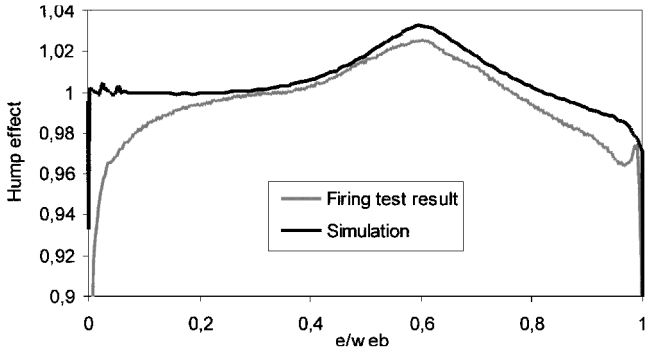

Fig. 9 Process B, hump effect (firing test result).

where r_b is the mean burning rate value, w_b is the web, p is the average effective pressure, and Ip_t is the integral over time interval of combustion pressure.

In the following discussion, the burning rate values are not absolute data but are given in comparison with a reference value.

The values obtained for the three processes can be compared because the local measurements to be presented show that the burning rate exponent is process independent. The ratio between the burning rate obtained for processes A and C and the value measured for process B is also computed. It appears that the grain manufactured using a casting without mandrel (process B) has a lower burning rate than the others of about 3%.

Figures 8 and 9 show the hump effect curves obtained for processes A and B. On those curves, the hump effect is the ratio between practical and theoretical pressure evolution. It is plotted vs percent burned web. They are quite different, and the curve obtained for process B is characteristic of grains cast without a mandrel.

Figures 10–13 show the profiles of the radial burning rate along the web for the three processes. For the three-points casting, the profiles under the casting point and in the knit line are given. Those results are obtained by ultrasonic measurements. Similar to the hump effect, the profiles are very dependent on the process. Overall, the radial burning rate profile is directly related to the hump effect. In Figs. 14 and 15, the longitudinal burning rate profiles along the height of the grain are presented for processes A and B. In both cases, the profile is quite constant. Those results are discussed in more detail in the next section.

Concerning more precisely the three points casting, we obtain very different profiles under the casting points and in the knit line.

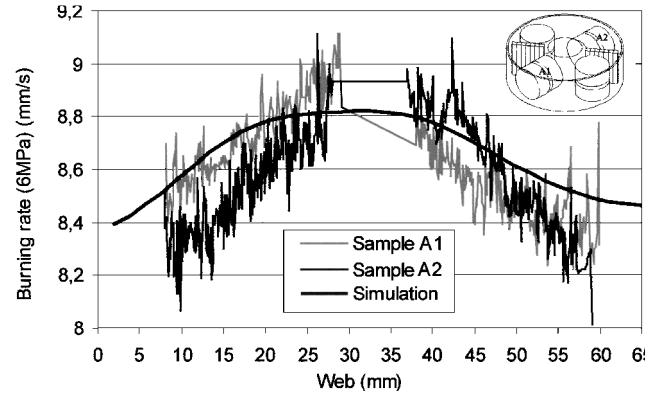

Fig. 10 Process A, radial burning rate along the web (ultrasound results).

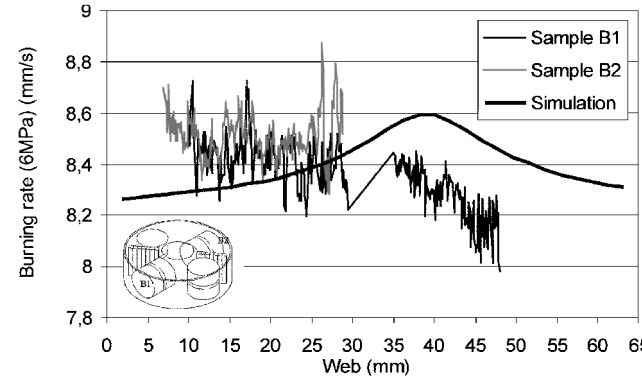

Fig. 11 Process B, radial burning rate along the web (ultrasound results).

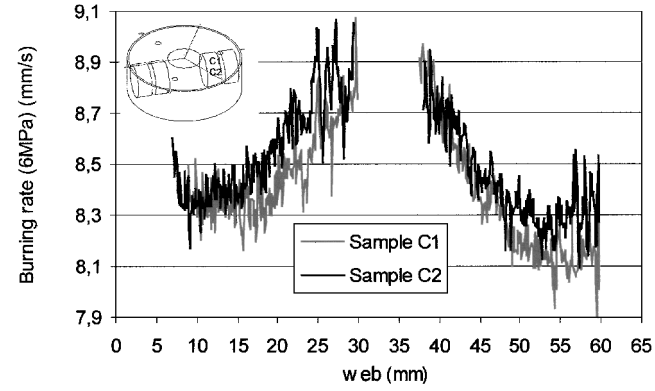

Fig. 12 Process C, radial burning rate along the web under a casting point (ultrasound results).

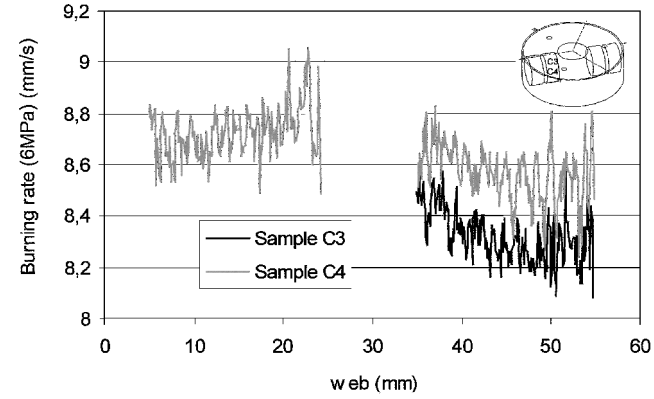

Fig. 13 Process C, radial burning rate along the web in the knit line (ultrasound results).

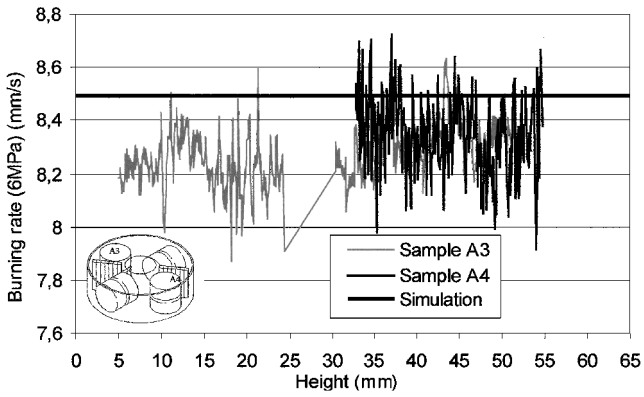

Fig. 14 Process A, longitudinal burning rate along the height (ultrasound results).

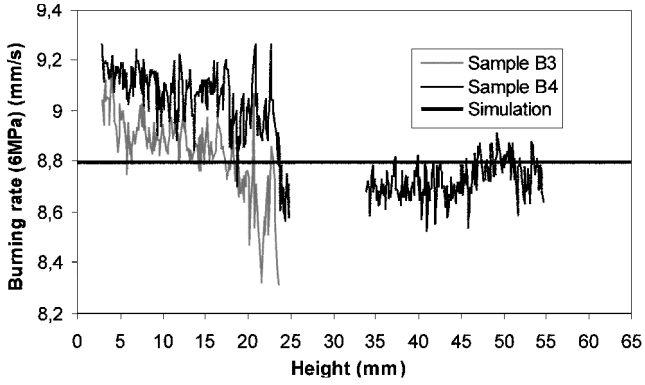

Fig. 15 Process B, longitudinal burning rate along the height (ultrasound results).

Furthermore, the mean value is 2.2% greater in the knit line. Those results are in agreement with the observations on large SRMs and particularly with the after firing measurements of thermal protection erosion. Indeed, in large SRMs manufactured using a three-points casting, a stronger erosion of thermal protections of the case along the knit lines is measured after firing tests. This effect is also presented in Fig. 16. It presents the evolution of the mean radial burning rate obtained by strand burner along the circumference (see Fig. 3 for the cutaway drawing).

B. Comparison of Experimental Results with Numerical Simulation

For processes A and B, numerical results are superimposed on experimental results in Figs. 10–11, 15–16, 17–18.

For process A (rotating casting with mandrel), the global behavior of the grain, shown by the hump effect in Fig. 8, is well predicted. The local behavior is also well simulated. The curves plotted in Figs. 10 and 14 show that our model is able to predict the shape of the radial burning rate variation along the web and the longitudinal burning rate variation along the length, as well as the ratio between the radial and the longitudinal burning rates (about 2%). The evolution of the longitudinal burning rate along the web is also well predicted, as presented in Fig. 17. To summarize, in the case of process A, our model is able to predict both global and local behavior of the grain and, furthermore, the anisotropic behavior of the propellant in accordance with processing.

The comparison, in the case of process B, is more difficult because, as is shown by the filling simulation and by the local measurements, the behavior of the grain is different from the bottom to the top, and as stated earlier, during the simulation, the stratification is supposed to be strictly periodical. Nevertheless, the comparison of computed and measured hump effect curves in Fig. 9 shows that the global behavior is well predicted except in the region where $e/eb = 0$. In this area, the difference between the experimental and

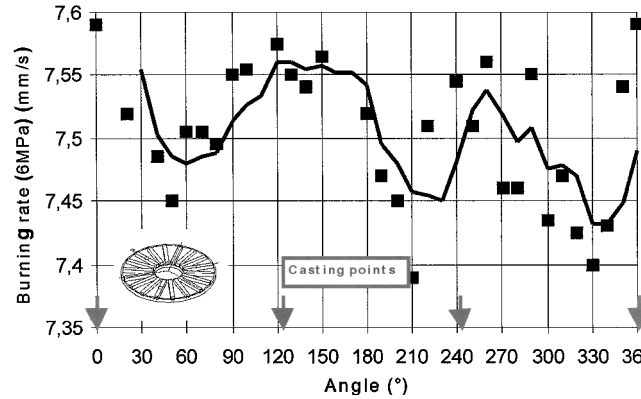

Fig. 16 Process C, mean radial burning rate around the circumference (strand burner result).

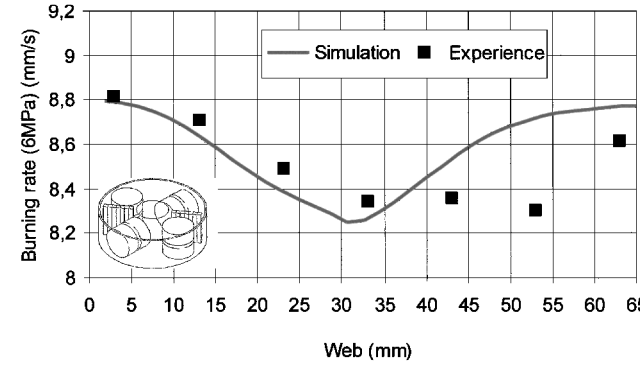

Fig. 17 Process A, longitudinal burning rate along the web (strand burner result).

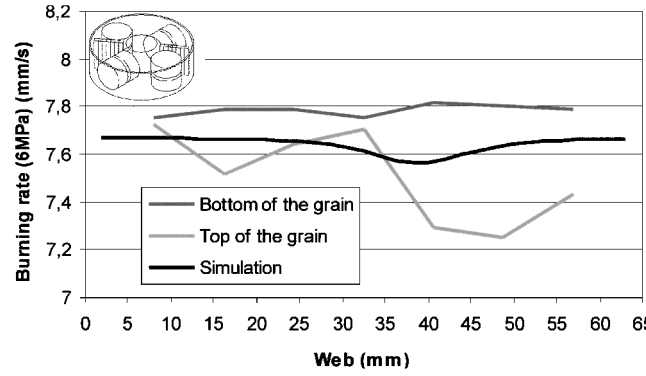

Fig. 18 Process B, longitudinal burning rate along the web (strand burner result).

the computed curves can be explained by that the ignition is supposed to be instantaneous in the simulation. In any case, the difference is not very large, and what is most important is that the general tendency between the two processes is quite well predicted. The agreement is not so good concerning the radial burning rate along the web (Fig. 11). This is partially because the measurement is obtained using two samples. Between them, there is an area in which no measurement is available. The problem is that the simulation predicts an increase of burning rate in this area, which is characteristic of this process, that we are unable to measure. Of course, this data gap would not exist if it was possible to use 70-mm-thick samples. Unfortunately, our test facility only enables 30-mm-thick samples. On the other hand, the comparison presented in Figs. 15 and 18 for the longitudinal burning rate is satisfactory. Furthermore, the ratio between the mean radial burning rate and the mean longitudinal burning rate is also well predicted (about 5%).

The comparison of processes is also illustrated in Table 1 through the mean burning rate ratio. The computed value (3.2%) is very close to the measured value (3.5%).

The comparison between measurments and computations presented on the two-dimensional configurations are in quite good agreement. The three-dimensional configuration will be simulated when the numerical model will have been validated. The first results we have obtained with this new model are promising,[20] but a few tests have to be performed.

IV. Conclusions

An experimental study has been performed on small-scale composite propellant grains to quantify the impact of manufacturing processes on ballistic performance. The global performance and the local behavior have been analyzed by means of firing tests and local measurements. The important influence of the manufacturing process on both global and local behavior has been clearly demonstrated.

The experimental results have been compared to the simulation results obtained using a new code developed at SNPE to compute surface burnback in composite propellant. The input values necessary for the simulation have been deduced from filling simulation and NMR visualization. The experimental and numerical results are in very good agreement.

Only the two-dimensional processes have been simulated. Indeed, the three-dimensional version of our code is still in development. The first results we have obtained are promising,[20] but a few tests have to be performed. When they are computed, the simulation of the three-points casted grain will be performed.

Our objective is to compute the performance of large-scale motors manufactured using complex filling processes to integrate in the simulation the effects usually integrated in hump effect and scale factor. The problem of the classical method is that it requires preliminary firing tests results. This new method will enable us to predict the performance of a SRM in the case of an anomalous filling and then help to decide if the segment may or may not be used. It will, of course, also enable us to predict the performance of a new motor, before the first firing test and taking into account the casting process.

Acknowledgments

This study has been supported by SNPE and the Centre National d'Etudes Spatiales within its Research and Technology Program.

References

[1]Le Breton, P., Ribéreau, D., Marraud, C., and Lamarque, P., "Experimental and Numerical Study of Casting Process Effects on Small Scale Solid Rocket Motor Ballistic Behavior," *Fifth International Symposium on Special Topics in Chemical Propulsion (5-ISICP)*, Stresa, Italy, June 2000.

[2]Chounet, G., Marraud, C., Giraud, E., and Carrasquet, P., "A5 Propellant Suspension: Rheology Control and Particle Migration During Casting," *Space Solid Propulsion Conference*, Rome, Italy, Nov. 2000.

[3]Thepenier, J., Ribéreau, D., and Giraud, E., "Application of Advanced Computational Software's in Propellant Grain Analysis: A Major Contribution of Future SRM Development For Space Application," International Astronautical Federation, IAF Paper 97-S.4.06, Turin, Italy, Oct. 1997.

[4]Davenas, A., and Thepenier, J., "Recent Progress in the Prediction and Analysis of the Operation of Solid Rocket Motors," International Astronautical Federation, IAF Paper 98-S.2.06, Melbourne, Australia, Sept.–Oct. 1998.

[5]Beckman, C. W., and Geisler, R. L., "Ballistic Anomaly Trends in Subscale Solid Rocket Motors," AIAA Paper 82-1092, 18th AIAA/ASME Joint Propulsion Conf., Cleveland, OH, 1982.

[6]Geisler, R. L., "Recent Observations of Solid Propellant Ballistic Anomalies Resulting from Propellant Processing," *Proceeding of 1992 JANNAF Propulsion Meeting*, Feb. 1992.

[7]Ribéreau, D., Le Breton, P., and Giraud, E., "Solid Rocket Motor Three-Dimensional Surface Burnback Computation Using Mixes Stratification Deduced from Three-Dimensional Grain Filling Simulation," AIAA Paper 99-2802, 35th AIAA/SAE/ASME/ASEE JPC, Los Angeles, CA, June1999.

[8]Davenas, A., *Solid Rocket Propulsion Technology*, Pergamon, Oxford, New York, 1993.

[9]Kallmeyer, T. E., and Sayer, L. H., "Differences Between Actual and Predicted Pressure–Time Histories of Solid Rocket Motor," AIAA Paper 82-1094, Cleveland, OH, June 1982.

[10]Heister, S. D., and Davis, R. J., "Predicting Burn Time Variations in Solid Rocket Motors," AIAA Paper 90-2736, Orlando, FL, July 1990.

[11]Uhrig, G., Ribéreau, D., Hiss, A., Brauner, C. M., Namah, G., and Suys, O., "Processing Effects on Ballistic Response of Composite Solid-Propellant Grains," AIAA Paper 95-2585, San Diego, CA, July 1995.

[12]Le Breton, P., Ribéreau, D., and Godfroy, F., "SRM Performance Analysis by Coupling Bidimensional Surface Burnback and Pressure Field Computations," AIAA Paper 98-3968, Cleveland, OH, July 1998.

[13]Abgrall, R., "Numerical Discretization of Boundary Conditions for First Order Hamilton Jacobi Equations," TR 96031, Mathemathiques Appliquées de Bordeaux, Bordeaux, France, Dec. 1996; also Soumis à Communications in Pure and Applied Mathematics.

[14]Abgrall, R., "Numerical Discretization of First Order Hamilton Jacobi Equations on Triangular Meshes," *Communications in Pure and Applied Mathematics*, Vol. 49, Dec. 1996, pp. 1339–1373.

[15]Grandall, M. G., and Lions, P. L., "Viscosity Solutions of Hamilton Jacobi Equations," *Transactions of the American Mathematical Society*, Vol. 277, No. 1, 1983.

[16]Barles, G., "Solutions de viscosité des équations de Hamilton-Jacobi," *Mathématiques et Applications*, Springer-Verlag, Berlin, Vol. 17, 1994.

[17]Krieger, I., "Rheology of Monodisperse Lattices," *Advances in Colloid Interface Science*, Vol. 3, 1972, pp. 111–136.

[18]Phillips, R. J., Armsttrong, R. C., and Brown, R. A., "A Constitutive Equation for Concentrated Suspensions that Accounts for Shear Induced Particle Migration," *Physics of Fluids A*, Vol. 4, No. 1, 1992, pp. 30–40.

[19]Tetlow, N., Graham, A. L., Ingber, M. S., Subia, S. R., Mondy, L. A., and Altobelli, S. A., "Particle Migration in a Couette Apparatus: Experiment and Modelling," *Journal of Rheology*, Vol. 41, No. 2, 1998, pp. 307–327.

[20]Le Breton, P., Ribéreau, D., and Ballereau, S., "Study of Casting Process Effects on P230 SRM Performance by 3D Surface Burnback," Space Solid Propulsion Conf., Rome, Italy, Nov. 2000.